JOURNAL OF PROPULSION AND POWER
Vol. 27, No. 2, March–April 2011

# Flow Characteristics of Small-Sized Supersonic Inlets

Hyoung Jin Lee* and Bok Jik Lee*
*LIG Nex1, Co., Ltd., Daejeon 305-804, Republic of Korea*
and
Sung Don Kim† and In-Seuck Jeung‡
*Seoul National University, Seoul 151-742, Republic of Korea*

DOI: 10.2514/1.46101

**The flow characteristics were investigated for two types of small-sized supersonic inlet models: rectangular and axisymmetric inlets. The two models were designed by the same method and are of similar size, with a total length of about 160 mm. The flow phenomena that were generated at the stable and unstable operating conditions of both models are visualized and discussed in detail. The main flow feature for stable operation is the existence of a shock train induced by the shock boundary-layer interactions. The results show that the shock-train shape and position are varied along with the upstream and area ratios, which strongly impact the downstream flow and total pressure recovery. For unstable operation, various buzz phenomena are observed for different area ratios. The results indicate that the buzz phenomenon of the small-sized inlet is identical to that of a large inlet, but the small inlet can be easily affected by the presence of a separation bubble. Although the shapes of the inlets are different, the base frequencies of a big buzz for both models are very similar. The role of the separation on the compression surface in the buzz process of the small-sized inlet is shown.**

## Nomenclature

$A_e$ = geometrical throat area of exit jet
$A_t$ = cross-sectional area at throat section of inlet
$Ai$ = cross-sectional area at entrance of test model
$c$ = speed of sound
$f_n$ = fundamental frequency of inlet buzz
$L$ = length of inlet duct
$M$ = Mach number
$M_s$ = Mach number immediately upstream of terminal shock
$M_\infty$ = Mach number at freestream
$P$ = surface pressure
$P_{\mathrm{RMS}}$ = root-mean-square pressure
$P_{\mathrm{to}}$ = freestream total pressure.
$Re$ = unit Reynolds number, dimensionless
$u$ = local velocity
$\eta_{\mathrm{Pt}}$ = total pressure recovery
$\eta_{\mathrm{Pt}_l}$ = total pressure loss ratio
$\rho$ = local density

## I. Introduction

THE function of a supersonic inlet is to provide a subsonic flow to the combustor at a desired velocity, a high total pressure recovery, and a uniform and stable flow. Thus, the supersonic inlet is closely associated with engine performance and is considered one of the most important elements in a supersonic airbreathing engine [1,2]. For this reason, many studies on this topic have been conducted over the past five decades, but research is still required to solve some aspects of the design of the supersonic inlet. This is because complex flow phenomena such as shock boundary-layer interactions (SBLIs) and unstable shock motions around the supersonic inlet are not fully understood at present. Thus, it is very important to observe all the typical flow phenomena that can prevail both inside and outside the inlet.

Several studies have helped to establish an understanding of the relationship between the inlet performance and various physical phenomena, such as the effect of pseudoshock on inlet performance [3–17] and the buzz phenomenon, together with the mechanism that initiates it [18–30]. However, although all of these results are very noteworthy, the results are limited because they are generally deduced from fragmentary images of the inlets and local pressure data. Under conditions of unstable operation, there exist no visualized results that fully reveal the features of internal flow. Indeed, even for the case of stable operation, not many visualized results have been published to date. In addition to these general issues, it is necessary to consider the effect of the inlet size. Several studies on small-sized solid fuel ramjets (SFRJs) have been conducted toward the goal of designing a gun-launched projectile for the past 10 years [31–33]. However, most of those studies focused on either the design of a combustor or the combustion phenomenon of SFRJs, while studies on inlets have rarely been reported. The successful design of such a projectile requires detailed knowledge of the performance at the subsystem level because complex physical phenomena exist due to interactions between the subsystems [32]. Therefore, studies on small-sized inlets are still needed to confirm whether or not their flow characteristics are the same as those of a large supersonic inlet, such as a conventional ramjet intake.

This study aims to uncover the flow characteristics of inlets and confirm extant findings that have been limited to plausible diagrams by showing detailed flow-visualization images for all regions of the inlet across the entire operation. In addition, we aim to understand the flow characteristics of the small-sized inlet. Our investigations are based on experiments conducted with the conventional, blowdown, supersonic wind tunnel at the Aerospace Propulsion and Combustion Laboratory at Seoul National University. Numerical simulations were also conducted to aid the experimental data. For this study, two types of similar-sized inlet models, axisymmetric and rectangular, which exhibit self-starting characteristics, were designed using the same method [2]. The total length of both models was about 160 to 170 mm [34]. The scale and the shape of our axisymmetric model are very similar to those of the SOFRAM [31]. The experimental data

---

Received 23 June 2009; revision received 7 November 2010; accepted for publication 15 November 2010.

*Research Engineer, PGM Research and Development Laboratory; Seoul National University, School of Mechanical and Aerospace Engineering, Seoul 151-742, Republic of Korea. Member AIAA.

†Research Engineer; Seoul National University, School of Mechanical and Aerospace Engineering, Seoul 151-742, Republic of Korea. Member AIAA.

‡Professor, Department of Aerospace Engineering, Institute of Advanced Aerospace Technology; enjis@snu.ac.kr. Associate Fellow AIAA (Corresponding Author).

were obtained through static pressure measurements and a high-speed schlieren visualization technique.

## II. Literature Review

### A. Stable Operation

Most of the previous investigations on SBLIs were conducted in constant-area channels where the effects associated with a sustained, postshock pressure gradient were either totally absent or greatly suppressed; the findings of these studies are summarized in [3]. Thus, even though there are a large number of studies on SBLIs, only a few of the published experiments are directly applicable to inlet flows [9]. Several experimental [4–13] and numerical investigations [14–17] have been reported on terminal shocks, and a comprehensive review was given by Hamed and Shang [11] on the SBLI that is pertinent to predicting the flows in supersonic inlets. The typical trends in terminal shock presented by Sajben and Kroutil [7] are divided into four patterns on the basis of the Mach number $M_s$ that prevails immediately upstream of the terminal shock in the subsonic diffuser. When the $M_s$ is smaller than 1.3, the structure is a single normal shock that shows some curvature near the walls. Above this value, shock-induced separation occurs, and the single shock transmutes into patterns of bifurcation. For $M_s$ values greater than 1.6, a normal or oblique shock train appears. The classification system given by Sajben et al. is similar to that for constant-area ducts, but the shape of the shock train is completely different. Additionally, Bogar et al. [8] and Sajben et al. [9] found that two or three separated patterns can occur for the same downstream condition, depending on the history of the flow. Mahoney showed the effect of the length of the pseudo-shock on the total pressure recovery in the supersonic inlet [2].

### B. Unstable Operation (Inlet Buzz)

The stability of an inlet flow at various flight conditions is one of the major considerations in the design of supersonic inlets. Theoretically, the stable operation of an inlet is achieved at the design condition. However, under certain flight conditions, the regulation of the engine thrust usually entails a reduced consumption of mass flow at the inlet. When the rate of the entering mass flow falls below a certain value, supersonic inlets often encounter the problem of aerodynamic instability, which is called an inlet buzz. During inlet buzz, supersonic inlets exhibit considerable shock system oscillations in front of the inlet and large corresponding fluctuations in the pressure and mass flow downstream [18–30].

The first studies of inlet buzz were undertaken by Ferri and Nucci [19] and Dailey [20], following the observations of Oswatitsch [18]. The initiation mechanisms that they suggested have been confirmed by many subsequent studies. Buzz is classified into two types on the basis of the initiation mechanism: the Ferri type, where buzz is initiated by the shear layer that arises inside the inlet duct, and the Dailey type, where the buzz is triggered by the obstruction that is caused by separation on the compression surface. Since these pioneering studies, many investigations have been conducted on different inlet configurations. Several experimental studies by Hermann [21], Sterbentz and Evvard [22], Trimpi [23], Connors and Wollett [24], and Nagashima et al. [25], among others, focused on flow without a cone separation or a Ferri-type buzz. In particular, Nagashima et al. [25] depicted the oscillatory motion of external shock using schlieren images recorded by a high-speed camera. For Dailey-type buzzes, Hongprapas et al. [26] confirmed the influence of the separated flow inside the inlet by using plausible patterns of the internal flow that were based on measurements taken during stable operation. Lu and Jain [27] conducted numerical simulations using the RANS equation and the Baldwin–Lomax turbulence model; their results showed that the buzz cycle is attributed to both the instability of the local flow around the entrance and the acoustic resonance modes that appear inside the plenum chamber. Fisher et al. [28] carried out experimental studies using a rectangular external-compression inlet, and they observed two different types of buzzes, which they termed little buzz and big buzz on account of the different flow conditions. Their experimental results suggested that little buzz is triggered by a shear layer that enters inside the cowl lip, whereas big buzz is related to a separation on the compression surface. Recently, Trapier et al. [29,30] conducted experimental and numerical studies for a mixed-compression rectangular inlet model, similar to the model examined by Fisher et al. They also observed little buzz and big buzz for various Mach numbers (1.8–3.0) and more clearly established Fisher et al.'s [28] findings regarding the mechanisms that trigger buzzes.

## III. Experimental and Numerical Setup

### A. Supersonic Wind Tunnel

The experiment was conducted using a conventional, supersonic, blowdown wind tunnel. The facility allows for approximately 10 s of runtime. The test section is square-shaped and has a size of 109 × 109 mm. A two-dimensional converging–diverging supersonic nozzle with a Mach number of 2.5 is located upstream of the test section. The measured turbulence level of the freestream is about 4.2% at the test section. The total flow conditions at the settling chamber are as follows: the total pressure is 950 kPa, the total temperature is 300 K, and the unit Reynolds number is $7.6 \times 10^7/\mathrm{m}$.

### B. Design of Test Model

Two types of inlet models are used in the present study, but the design method is the same for both models and is based on [2]. Drawings and photographs of the inlet models are given in Fig. 1. The axisymmetric model is a generic mixed-compression inlet, as shown in Fig. 1a. According to Oswatitsch's results [35] for the axisymmetric model, when one cone is used in the inlet model, the optimal half-cone angle is 30° for a Mach number of 2.5 in view of the total pressure recovery. After the half-cone angle had been decided, the height of the inlet throat was determined through a simple mass-conservation calculation so that the entrance flow was not choked at the throat. The connection between the compression surface and the throat is designed to have a curved surface with a radius that is four times the throat height, according to [2]. The calculated inlet throat height is 2.1 mm, the throat length is 5 mm, and the total length is 169 mm. The angle of the subsonic diffuser is 5°.

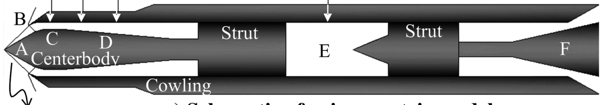

**a) Schematic of axisymmetric model**

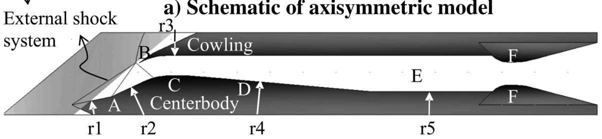

**b) Schematic of rectangular model**

A : Supersonic diffuser B : Cowl lip C : Throat D : Subsonic diffuser
E : Plenum chamber F : Plug to change backpressure or area ratio
a1~a4, r1~r5 : Surface static pressure measuring stations

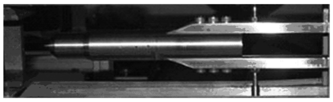

**c) Photograph of axisymmetric model**

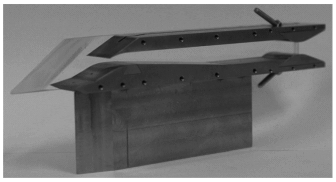

**d) Photograph of rectangular model**

**Fig. 1 Schematics and pictures of the experimental model.**

The rectangular model is designed by the same method, but the external compression is achieved by two ramps, as shown in Fig. 1b. The two ramp angles are decided on the basis of maximizing the total pressure recovery using one-dimensional theoretical calculations. The angles calculated are 12 and 25° for the freestream Mach number of 2.5. The remaining design parameters are determined in the same manner as for the axisymmetric model: the inlet throat height is 6.1 mm, the throat length is 5 mm, the angle of the subsonic diffuser is 5°, and the total length is 159 mm, while the width of rectangular model is 20 mm. Unlike the axisymmetric model, it is possible to visualize the internal flow in the rectangular model, and Plexiglas is used for a pair of sidewalls for this purpose.

All the design methods for the two models are the same, but the location of the cowl lip for the external oblique shock is varied so that its effect can be observed. As shown in Figs. 1a and 1b, the external oblique shock system (denoted by the lines on the compression surfaces) is located inside (axisymmetric model) and outside (rectangular model) the cowl lip, respectively. The diameter of the cowl lip is 13.7 mm in the axisymmetric model, and the height of the cowl lip is 12.9 mm in the rectangular model. Figures 1c and 1d illustrate the axisymmetric and rectangular models, respectively, installed in the wind tunnel.

### C. Experimental Data Acquisition

Experimental data were obtained through static pressure measurement and flow visualization using schlieren and shadow techniques. For the axisymmetric model, static pressure measurements were obtained at four stations on the inside surface of the cowling, as shown in Fig. 1a. The pressure was measured at the throat (a1), the subsonic diffuser (a2 and a3), and the plenum chamber (a4). For the rectangular model, the pressure was measured at five stations: two compression ramps (r1 and r2), the throat (r3), the subsonic diffuser (r4), and the plenum chamber (r5), as shown in Fig. 1b. Piezoresistive type dynamic pressure sensors (Keller and Swiss), which have the accuracy of 0.25% for a full scale of 10 bar, were used and sampled at 10 kHz using an automated data-acquisition system. The tube-fitting method was adapted due to the small size of the test model. For the axisymmetric model, there was no difficulty in measuring the dynamic pressure because the tubes were sufficiently short. However, for the rectangular model, the tube was too long. Thus, the absolute pressures could not be exactly measured during the unstable operation, but the model frequency was correctly detected. The detected frequency was verified using the images recorded for the terminal shock movements using a high-speed camera.

Schlieren or shadowgraph flow visualization is a well-established technique that is used to capture the formation of external and internal shocks at an inlet [36]. During stable operation, flow-visualization pictures were taken by a high-resolution charge-coupled device camera with a shutter speed of $1/8000$ s. For unstable operation, movies and images were recorded using a high-speed camera (Ultima APX and Photoron) that operated at 6000–10,000 frames per second. In this study, we attempt to synchronize the video and pressure data in the case of unstable operation.

### D. Test Procedure

The inlet operating conditions were varied by changing the position of the backplug, which controlled the throat area of the exit jet; see part F (plug) in Figs. 1a and 1b. The position of the backplug is identified by the area ratio (AR), which is defined as the ratio of the geometrical throat area of the exit jet $A_e$ to the cross-sectional area at the throat section of the inlet $A_t$. These experiments were conducted for AR values ranging from 0.316 to 1.5.

### E. Numerical Methods

Numerical simulations were conducted using the Reynolds-averaged Navier–Stokes (RANS) equation with the Menter–shear-stress-transport turbulent model [37]. Two-dimensional and axisymmetric analyses were conducted to confirm the base phenomenon and reduce the computational cost. Steady and unsteady simulations were conducted in accordance with the flow conditions. The equations were solved by the well-known Jacobi iterative implicit time-marching scheme [38] and Roe's flux difference splitting [39] using the Osher–Chakravathy gradient limiter [40], which exhibits good spatial accuracy up to the third order. The Jacobi-point iterative method has first-order time accuracy for unsteady simulations. The steady-state solution of the critical mode was used as the initial condition for the unsteady simulation. For the unsteady simulations, the time step was of $10^{-7}$ s and the results were sampled at every 0.1 ms.

The inflow boundary conditions were specified in terms of the unperturbed freestream conditions and were completely specified during the solution procedure. Since all of the test cases considered a supersonic freestream, the fixed upstream boundary conditions were empirically correct. For the outflow boundary condition, a no-gradient extrapolation was set at the exit due to the supersonic flow induced by the plug that was used in the experiments. The boundary conditions for the walls, such as the centerbody and cowl surface walls, were treated as no-slip boundaries by setting the velocity components on the walls to zero and employing adiabatic conditions.

The computational domain comprised an internal flow region that contained most of the essential flow structure and an external flow region that became important when the flow spilled over the cowl lip for the unstable operating regimes. The structured grid was applied for the computational domain and the total number of grid cells was about 340,000 for the rectangular model and 350,000 for the axisymmetric model. Figure 2 shows an example of grid for the rectangular model. For the best results, all cell centers at the wall were located well within the laminar sublayer ($y^+ \sim 1$). Therefore, very fine grids were located near wall boundaries, which included 180 points for the rectangular model and 120 points for the axisymmetric model in the directions of the walls. A simple grid-independence study was performed by increasing the grid numbers by 50% in the axial direction and 30% in the height or radial direction. The pressure valves and the terminal shock position are almost identical for the steady-state flowfields obtained from these two grids.

## IV. Results and Discussion

### A. Overall Operation

The results of the surface static pressure measurements, normalized by the freestream total pressure $P_{t0}$, are shown for both experimental models in Fig. 3. Plots of the time-averaged pressures for each measuring station against the AR are shown. The time-averaged pressures are useful for observing the overall flow trends, but they are not meaningful by themselves for unstable operation. The static pressure trends are divided into five modes of flow operation, depending on the position of the terminal shock. The operation regimes are subdivided into two segments, stable and unstable, depending on the operating mode of the inlet; the stable and unstable regimes are denoted by arrows in Fig. 3. The stable regime ranges from supercritical (I) to critical (II); in this regime, the inlet operates normally without severe shock oscillations, as the terminal shock is located inside the inlet duct. Only very weak terminal shock oscillations are observed for the stable regime. The subcritical (III), buzz (IV), and unstart (V) modes are included within the unstable operation regime; in this regime, a terminal shock is only observed near the inlet duct, or strong shock oscillations are observed throughout all of the regions of the inlet. Figure 4 shows the shadow

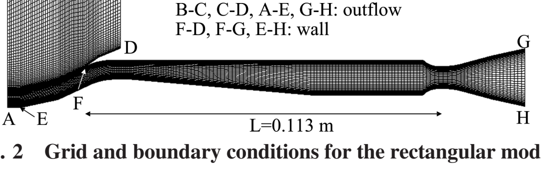

**Fig. 2 Grid and boundary conditions for the rectangular model.**

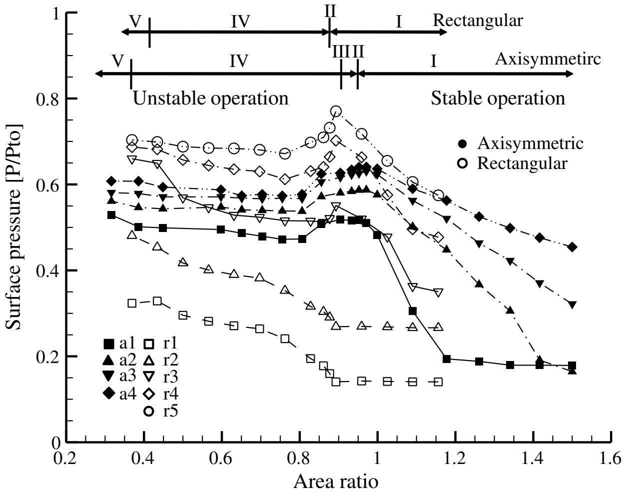

**Fig. 3 Surface-pressure results and the operation regime.**

images that indicate the external shock system and correspond to the five operating modes of the axisymmetric model. The pressure of the plenum chamber gradually increases as the AR decreases and reaches a maximum value at the critical point. Then, the pressure suddenly decreases at the point when a big buzz is initiated in both models. The overall flow trends for both models are similar, but the subcritical-mode regime differs for the two models due to the different location of external shock system. A more detailed classification of each operational mode can be defined as follows.

For modes I–II (supercritical–critical), the terminal shock exists within the inlet, and the formation of the external shock is invariant with the AR. The downstream static pressure rises with decreasing AR, which is typical behavior for a supercritical mode, wherein the exit jet flow closes down and the terminal shock or intensified shock train moves upstream. For the axisymmetric model, ARs that exceed 0.999 belong to this mode, but for the rectangular model, ARs that exceed 0.893 belong to this mode. Figure 4a presents the images for these modes.

For mode III (subcritical or little buzz), when the AR is lower than that for the critical mode, the terminal shock oscillates near the cowl lip, as shown in Fig. 4b, and the inlet regulates the entering mass flow through the spillage of flow. For this mode, the vortex sheet is generated by the interaction of terminal shock and external shock, which induce the inlet instability. Although it is not large, the terminal shock continuously oscillates near the cowl lip. Some authors have classified this oscillatory shock motion in subcritical operations as a little buzz [28–30]. For the axisymmetric model, the external shock system is located inside the cowl lip. Thus, the vortex sheet that can induce instability is generated at higher AR, and the subcritical mode can start at higher AR. Operations at ARs of 0.955 and 0.933 belong to this mode for the axisymmetric model. The axisymmetric model had some AR values that only produced the subcritical mode, while the rectangular model did not have any AR values that produced the subcritical condition. For the rectangular model, even when the AR was slightly reduced from the value for the critical mode, a big buzz was intermittently initiated. For the case of the rectangular model, the instability can be induced only when the terminal shock moves upstream cowl lip by high backpressure, because the external oblique shocks are located outside the cowl lip. Thus, an inlet buzz can be initiated easily at subcritical mode, because the terminal shock can be affected more easily by random pulse of backpressure or accumulation process.

For mode IV (buzz), an inlet buzz is produced in this regime, as indicated by large oscillations in the shock wave and large fluctuations in the static pressures. In this regime, a big buzz of both models is initiated intermittently or continuously as the AR varies. As Fig. 4c confirms, during buzz operation, a separation region on the compression surface and another oblique shock generated in the separation region are apparent. For the axisymmetric model, operating at AR values between 0.386 and 0.904 produces the buzz mode, while operating at ARs between 0.501 and 0.877 produces the buzz mode for the rectangular model.

For mode V (unstart), as shown in Fig. 4d, the terminal shock detaches from the inlet and the inlet is totally unstarted. Under this condition, all of the regions of the inlet are preserved at a subsonic condition and the pressures at all of the stations are somewhat similar. Operations at an AR of 0.316 for the axisymmetric model and at ARs below 0.368 for the rectangular model belong to this mode.

### B. Stable Operation (from Supercritical to Critical Modes)

When the supersonic inlet exhibits stable operation, the most important flow features are the SBLIs that are always present inside inlets, since their detailed forms affect the structure of the terminal shock system of the inlet. The boundary layer on the wall surface of the inlet interacts with the shock, creating a shock train and a pseudoshock with a higher Mach number. Sajben and Kroutil [7], Bogar et al. [8], and Sajben et al. [9] classified such shock trains into four kinds based on the Mach number $M_s$ that prevails immediately upstream of the terminal shock in the subsonic diffuser. Similar results were obtained in this study for both small-sized models. Experimental and numerical schlieren images were suggested to examine the shock-train patterns for different external shock systems in detail.

#### *1. Rectangular Model*

Figures 5–7 present experimental and numerical results for the rectangular model. Figure 5 shows the experimental and numerical schlieren images. Figure 6 gives the distributions of the static pressure normalized by the freestream total pressures for different ARs. The numerical and experimental results agree relatively well with each other, although the results obtained from the two-dimensional numerical analyses give overestimations at low AR values. It is considered that this difference might be induced by the three-dimensional effect and accuracy of AR because the test model is very small. Although the two sets of results differ slightly for low ARs, the differences are not large enough to adversely impact the aim of this study, which is to observe the flow characteristics inside the inlet diffuser. Figure 7 shows the numerical schlieren and Mach number images with an isocurve corresponding to a local Mach number of unity. Using this figure, we can distinguish between the supersonic and subsonic regions and examine the variation in the length of the shock train with the AR. Given the results in Figs. 5–7, the flow characteristics of the subsonic diffuser can be interpreted as follows.

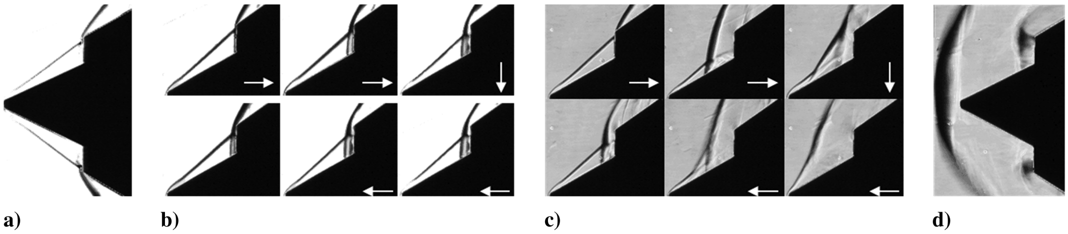

**Fig. 4 Shadow images of the operating mode for the axisymmetric model. (Note that white arrows represent the sequence of the images with recorded time.)**

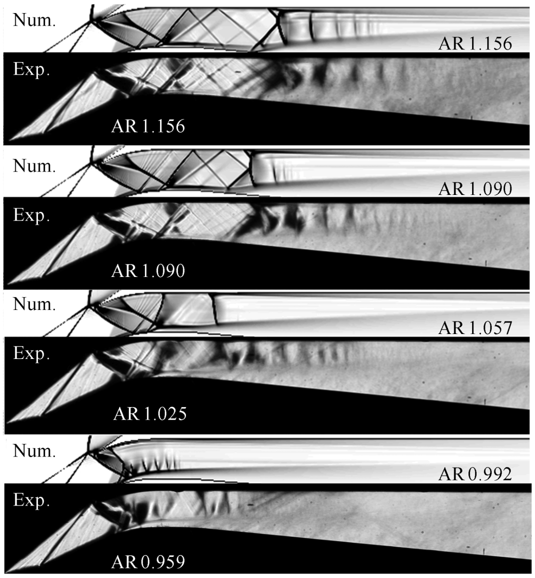

**Fig. 5 Schlieren images with AR values for the rectangular model.**

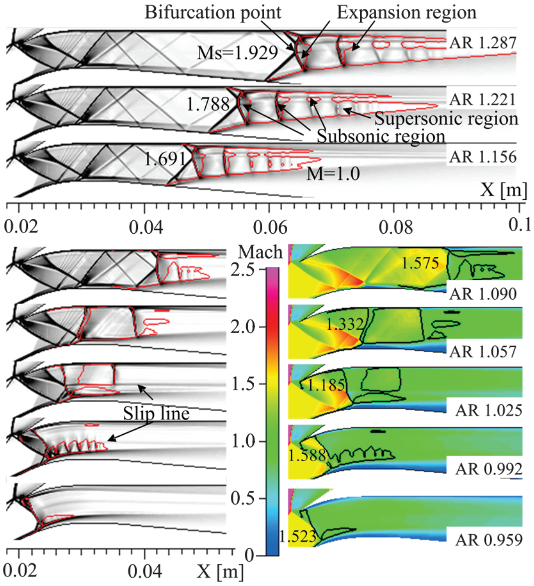

**Fig. 7 Numerical shock-train images with AR values for the rectangular model.**

1) The shock train is observed at AR = 1.287 at first. It is already known that the shape of the shock train is largely affected by the Mach number $M_s$ and the boundary layer just upstream of the shock train [10,16,17]. According to previous works involving a constant-area duct [10,16,17], a normal shock train, where the normal part of the leading shock is present, is observed when the $M_s$ is 1.5–1.7, whereas an oblique shock train, where the normal part of the leading shock disappears, is observed for $M_s$ values larger than 1.8–2.2. However, as shown in Fig. 7, the normal shock train is only observed when the shock train exists at the subsonic diffuser and the $M_s$ is 1.575–1.929. In Figs. 5 and 7, we can clearly see the lambda-shaped first shock wave with a vertical portion and two bifurcation points, while the second shock wave is concave toward the upstream direction. Unlike the results from the constant-area duct, the asymmetric oblique shocks are generated from asymmetric separation regions, and a distorted diamond-shaped expansion region exists immediately behind the normal part and rear leg of the first shock. These consecutive structures make up the asymmetric shock train in the subsonic diffuser. As the AR decreases, the $M_s$ also decreases and the number of shocks, the spacing between two consecutive shocks, and the length of shock train gradually decrease.

2) When the AR is decreased to 1.057 and 1.025, the terminal shock moves to the inlet throat, and it seems that a single normal shock exists on the inlet throat. This pattern seems similar to the results of Sajben and Kroutil [7], where the ranges of $M_s$ are 1.266–1.399 (AR = 1.057) and 1.083–1.287 (AR = 1.025). However, the boundary layer is much thicker at the centerbody-side surface of the inlet throat as the terminal normal shock intersects with the oblique shock that originated at the cowl lip. This causes the subsonic flow behind the normal shock to reaccelerate into a supersonic flow as the flow passage becomes narrower, and another single normal shock (as suggested by the numerical results) or another shock train (as experimentally observed) is generated in the subsonic diffuser, as shown in Figs. 5 and 7. The result suggests that it is not that the pattern of a shock train is determined by only $M_s$. As the AR further decreases, $M_s$ increases as the terminal shock moves to the expansion region near the cowl lip, but another shock train is not observed. However, a slip line is generated below an AR of 1.025, as the terminal shock interacts with the oblique shock that is generated from the cowl lip. Another small shock train is generated below the slip line because the compression and expansion waves are reflected in that region.

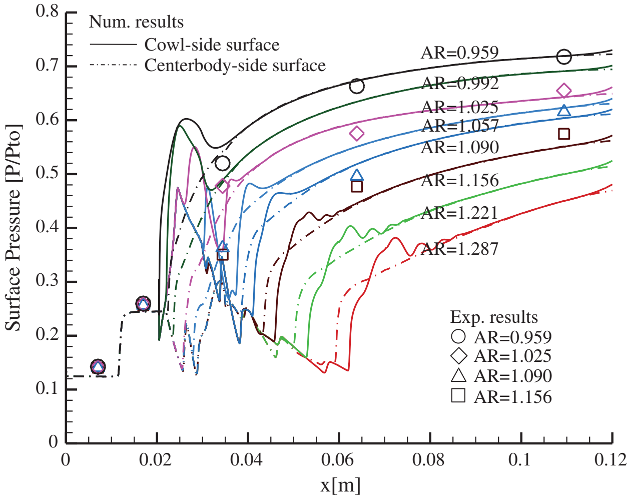

**Fig. 6 Surface static pressure distributions with AR values for the rectangular model.**

3) The static pressure distributions of the centerbody-side surface maintain a smooth and stable growth trend, but the pressure distributions of the cowl-side surface widely fluctuate at AR values above 1.156; the fluctuations are caused by asymmetric shock formations. The oblique shock that is generated from the cowl lip is reflected at the centerbody-side surface of the inlet throat, which greatly thickens the boundary layer on the centerbody side. On the other hand, the boundary layer that develops on the cowl-side surface is significantly thinner, because there are no major factors that can thicken the boundary layer of this surface, since the external oblique shocks are located outside the cowl lip. This asymmetrically distributed boundary layer is the main cause of the asymmetric shock train at the upstream region of the shock train. The oblique shock on the centerbody side is longer and stronger than that on the cowl side, which makes the boundary layer near the centerbody-side surface even thicker, resulting in a smooth surface-pressure distribution, as shown in Figs. 6 and 7. By contrast, because the supersonic core flow is deflected to the cowl-side surface, the surface pressures on this side are easily affected by the shock waves and expansion waves in the shock train, thereby producing large fluctuations in the streamwise direction. These fluctuations due to the shock train disappear below AR values of 1.090 since the shock train is no longer observed. Also, the pressure fluctuation is not observed, although a small shock-train region exists below the slip line at AR = 0.992 due to the thick boundary layer on the centerbody side. For the flow region following the shock train, the dominant flow processes include supersonic

mixing and subsonic diffusing; therefore, the surface-pressure distribution on the cowl side returns to a smooth trend and agrees with that of the centerbody side.

### 2. *Axisymmetric Model*

Figures 8 and 9 show the experimental and numerical results for the axisymmetric model, respectively. Figure 8 gives the distributions of the static pressure and Fig. 9 shows the numerical schlieren and Mach number results. The fluctuations of the surface-pressure distributions at $x = 0.06$ m and $x = 0.08$ m in Fig. 8 are due to the geometry of the backstep for the strut part of the model, as shown in Fig. 1a, and do not substantially affect the characteristics of the main flow or the shock train. According to the results in Figs. 8 and 9, the general features of the internal flow, as a function of the AR, are essentially the same as for the rectangular model except for some differences. The similar and differing flow features for both models can be interpreted as follows:

1) As shown in Fig. 9, unlike the results of the rectangular model, only the oblique shock train is observed when the shock train exists in the subsonic diffuser and $M_s$ is in the range 1.603–2.123. $M_s$ is very similar to that of the rectangular model. This result also suggests that the shape of shock train can be affected not only by the upstream Mach number but also by the diffuser shape, such as its diameter or height. Similar to the shape of a normal shock train, asymmetric oblique shocks are generated. However, the flow behind the bifurcation point of the leading oblique shocks has different features. For the case of the oblique shock train, the flow downstream of the bifurcation point is still supersonic. Thus, a compression region exists immediately behind the bifurcation point, wherein the flow is shaped by the separation bubble on the surface of the wall. In this study, when $M_s$ is sufficiently large (e.g., 2.123), the flow downstream of the bifurcation point retains its supersonic conditions at the narrowest part of the flow passage, beyond which a normal shock is observed. When $M_s$ is less than about 2.0, a normal shock is observed immediately behind the point of bifurcation. Compared with the case of a normal shock train, the region of supersonic mixing in an oblique shock train is much longer, because the region in which the flow easily can be subsonic, such as the region between two slip lines in a normal shock train, does not exist. The variation with the AR of the flow features of an oblique shock train is similar to that for a normal shock train.

2) The biggest difference is that the core flow is deflected to the centerbody-side surface for all AR values. In contrast to the rectangular model, the strong external oblique shock is located inside the inlet cowl and reflected on the cowl-side surface, which greatly thickens the boundary layer on the cowl-side surface. For this reason, an asymmetric boundary layer that is thicker on the cowl-side surface develops, and an asymmetric shock train is observed where the bifurcated-leading oblique shock is stronger on the cowl-side surface. Thus, the patterns of the shock train are unlike those in the rectangular model, as the surface-pressure distributions fluctuate on the centerbody-side surface. This conclusion is confirmed by the results of the rectangular model shown in Fig. 10, which show two numerical schlieren images and a local Mach number with different inflow Mach numbers $M_\infty$. The inflow conditions of the two images have the same total pressure, whereas the inflow Mach number is 2.5 in the first image and 3.0 in the other. The images are different from each other in terms of the overall shape of the shock structure, as the $M_s$ values are unequal due to the differing inflow Mach number. However, as mentioned previously, we can explain the asymmetric shock train that is generated from the asymmetric boundary layer. Compared with the results for $M_\infty = 2.5$, the external oblique shock for $M_\infty$ of 3.0 is reflected on the cowl-side surface, and the boundary layer becomes thick on that surface, which results in a different asymmetric shock train and a different core flow direction, explaining why the shapes of the asymmetric shock trains are different for the two models. Additionally, the oblique shock train that is generated in the rectangular model for $M_\infty = 3.0$ exhibits exactly the same flow characteristics as for the axisymmetric model.

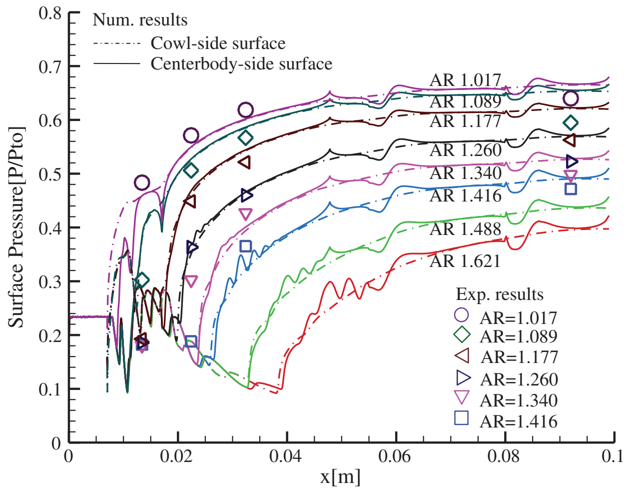

**Fig. 8 Surface static pressure distributions with the AR values for the axisymmetric model.**

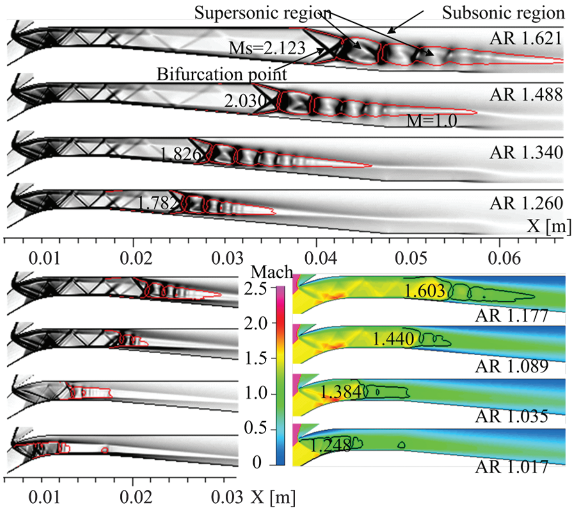

**Fig. 9 Numerical shock-train images with AR values for the axisymmetric model.**

### 3. *Comparison of Total Pressure Parameters*

For both models, Figs. 11–13 show the total pressure parameters, including the total pressure recovery and loss ratio. The total pressure parameters are estimated from numerical solutions in accordance with the following definitions.

Total pressure recovery:

$$\eta_{\mathrm{Pt}} = \frac{\int_A \rho u P_t \,\mathrm{d}A / \int_A \rho u \,\mathrm{d}A}{\int_{A_i} \rho u P_t \,\mathrm{d}A_i / \int_{A_i} \rho u \,\mathrm{d}A_i} \tag{1}$$

Total pressure loss ratio:

$$\eta_{P_{t_l}} = 1 - \eta_{P_t} \tag{2}$$

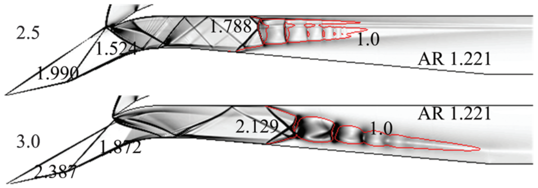

**Fig. 10 Comparison of shock train with different inflow Mach numbers for the rectangular model.**

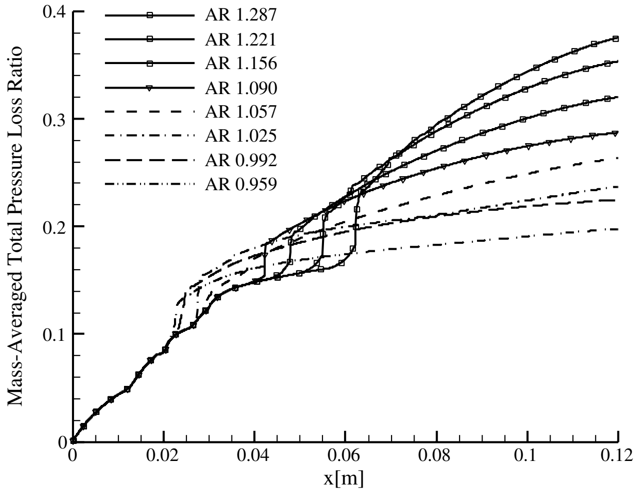

**Fig. 11 Total pressure loss with the AR values for the rectangular model.**

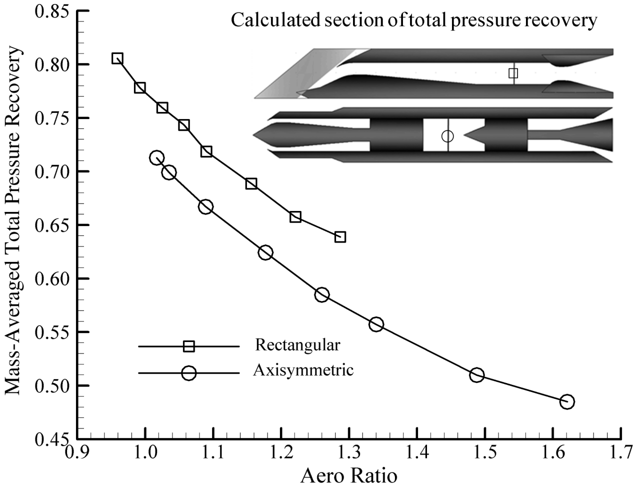

**Fig. 13 Mass-averaged total pressure recovery at the plenum chamber for both models.**

These parameters are mass averaged, which means that the total pressure is weighted by the local mass flux and integrated over the section.

Figures 11 and 12 show the variation of the total pressure loss ratio along the streamwise direction (the starting and ending points of the abscissa *x* refer to the starting point of the compression surface and the ending point of the plenum chamber of the inlet model, respectively) for both models. Figure 11 shows the typical characteristics of the total pressure loss in a normal shock train. The total pressure loss continuously increases in all the regions of the shock train, but a severe spike is generated at the leading normal shock portion, which is precisely the point of bifurcation. Another jump in the total pressure loss is not observed in the succeeding normal shock that lies behind the leading normal shock. For all of the normal shock trains, about 30% of the total pressure loss is generated at the first normal shock portion. Figure 12 shows the variation of the total pressure loss in an oblique shock train. Similar to the case of a normal shock train, the total pressure loss continuously increases in all of the regions, but a severe spike is not observed; only small jumps are generated at the normal shock portion of the two oblique shocks and not at the point of bifurcation. In both models, when the terminal shock moves to the inlet throat as the AR is reduced, the shock train intensifies into a normal shock. Furthermore, the total pressure loss is realized at the location of the normal shock, and there is little pressure loss downstream of the normal shock.

Figure 13 shows the variation of the mass-averaged total pressure recovery at the midsection of the plenum chamber (denoted by the line in the schematic diagram of the inlet) for both models. In both models, the total pressure recovery increases almost linearly as the AR value decreases, but its value for the rectangular model is larger than that for the axisymmetric model. There are two reasons for this discrepancy. While the Mach number at the cowl-lip section is nearly the same for both models (about 1.5), the axisymmetric model has one compression surface, whereas the rectangular model compresses the airflow through two wedges. Thus, the total pressure loss at the compression surface is greater for the axisymmetric model. Additionally, another total pressure loss is added in the axisymmetric model as the external oblique shock interacts with the detached cowl shock inside the inlet duct. Thus, we observe a jump in the total pressure loss at the cowl-lip section of the axisymmetric model. For this reason, when the inlet operates near the critical mode, the total pressure loss for the axisymmetric model is larger than that for the rectangular model, and the maximum total pressure recoveries are about 0.71 and 0.81 for the axisymmetric and rectangular models, respectively.

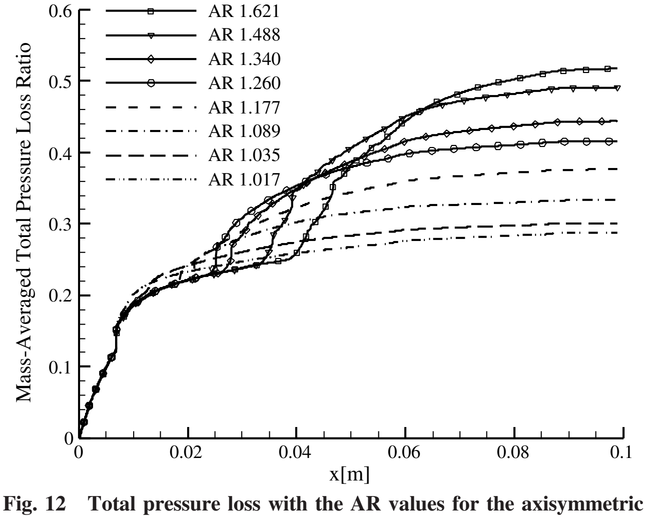

**Fig. 12 Total pressure loss with the AR values for the axisymmetric model.**

## C. Unstable Operation (Inlet Buzz)

An inlet buzz occurs when the shock system oscillates in front of the inlet under special conditions. A little buzz is observed when the inlet is operated at a subcritical mode. When the AR is lower than that of the subcritical mode, a big buzz is initiated for both models. A big buzz is initiated intermittently or continuously for various ARs. An intermittent buzz is observed for relatively larger ARs, while a continuous buzz is observed for the lower ARs. During the intermittent-buzz operation, a shock slightly oscillates near the cowl lip for a random duration that is on the order of 1 to 10 ms, as for the subcritical mode (little buzz); then, the shock system oscillates largely forward and backward for a random number of cycles (big buzz). On the other hand, during the continuous-buzz mode, there is no duration for which the shock system is situated near the cowl lip, and only the big buzz is initiated continuously and periodically.

### *1. Buzz Characteristics with Area Ratios*

Figure 14 shows the dynamic pressure profiles of the axisymmetric model, ranging from the subcritical to the continuous-buzz modes, over durations of 100 ms. As shown for the subcritical mode in Fig. 14a, small fluctuations in the pressure data are observable at all inlet stations ($P_{\mathrm{RMS}}/P_{\mathrm{to}} = 1.25\%$ at plenum chamber). As the AR decreases slightly from the value for the subcritical mode, the big buzz initiates intermittently and large pressure fluctuations are produced, as shown in Fig. 14b ($P_{\mathrm{RMS}}/P_{\mathrm{to}} = 3.6\%$ at plenum chamber). The onset frequency of the intermittent buzz that accompanies these large fluctuations increases as the AR further decreases. By contrast, the duration of the subcritical mode gradually decreases, as in Fig. 14c ($P_{\mathrm{RMS}}/P_{\mathrm{to}} = 6.0\%$ at plenum chamber). For

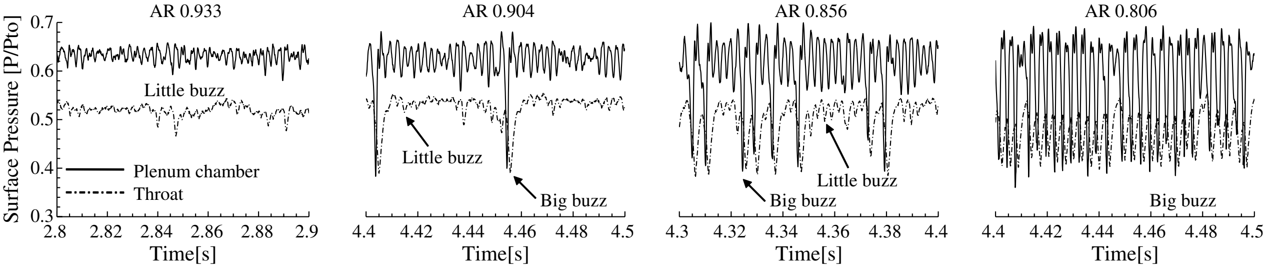

**a) Subcritical** **b) Intermittent buzz** **c) Intermittent buzz** **d) Continuous buzz**

**Fig. 14 Pressure from the subcritical to buzz modes for the axisymmetric model during a 0.1 s interval.**

the intermittent-buzz mode shown in Fig. 14c, the frequency of onset of the buzz is not constant and varies randomly, but its initiation frequency increases as the AR decreases. For example, the frequency of onset of the buzz is about 10–20 Hz at an AR of 0.904 and considerably varies at an AR of 0.856, from 25–50 Hz to about 100 Hz. When the AR is set below 0.806, the time for which the inlet operates at the subcritical mode disappears and only a big buzz is continuously initiated, as shown in Fig. 14d ($P_{\mathrm{RMS}}/P_{\mathrm{to}} = 8.6\%$ at plenum chamber). The normalized $P_{\mathrm{RMS}}$ value is very similar with the Trapier et al. experimental results [29], although the model size is largely different. The base frequency of the inlet is the same at all the stations for any given AR and changes from 312.5 to 447.8 Hz for the continuous-buzz mode as the AR decreases. However, its amplitude is not the same across stations: the amplitude in the plenum chamber is the largest, which means that the pressure fluctuation is largest in the plenum chamber. As shown in Fig. 14, changing the AR does not affect the amplitude of the surface-pressure fluctuations, but it affects the base frequency of the buzz. Figure 15 presents the spectrogram of the pressure signal at the plenum chamber. The assumption that the ARs of Fig. 14 are changed at every 0.1 s is applied in the pressure data of Fig. 15 to understand how the energy of the process is decomposed over time and frequency. The frequency levels of little and big buzzes are almost identical, and this result implicates that the buzz is strongly related with the acoustic stimulation.

This phenomenon is observed in the rectangular model as well. Figure 16 shows the dynamic pressure traces for the plenum chamber of the rectangular model. The subcritical mode appears first at an AR of 0.877, but the buzz phenomenon is also intermittently observed at the same AR. For the intermittent-buzz mode at an AR of 0.877, the onset of the buzz is randomly observed for frequencies in the range 15–100 Hz, as shown in Fig. 16b. When the AR drops below 0.877, the intermittent buzz changes into a continuous buzz. Compared with the results for the axisymmetric model, the range of AR values for which the mode changes from subcritical or critical to continuous buzz is narrower. This is because the range of AR values for which the subcritical mode is preserved is wider for the axisymmetric model due the external shock system inside the cowl lip. The base frequency increases from 252.2 to 444.7 Hz for the continuous-buzz mode as the AR decreases. Similar to the results for the axisymmetric model, for any given AR, the base frequency is the same at all stations during the buzz, implying that the whole inlet is affected by the massive shock motion during the buzz.

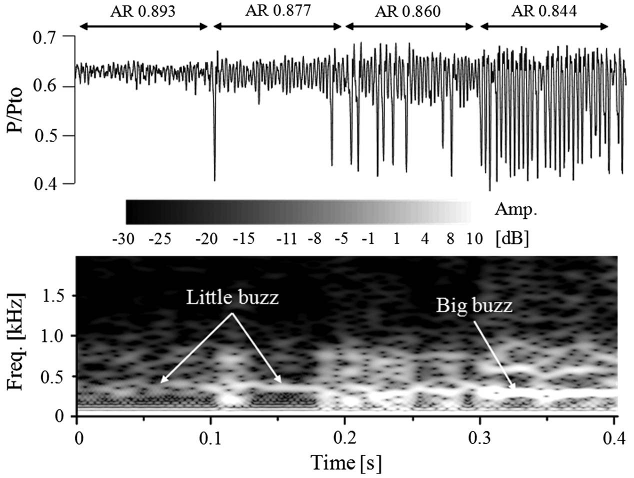

**Fig. 15 Spectrogram of pressure signal at plenum chamber for the axisymmetric model.**

### 2. *Detailed Analysis of a Buzz Cycle*

Figure 17 presents the surface-pressure histories and shadowgraph images obtained from a high-speed camera that records 6000 frames per second at an AR of 0.704 for the axisymmetric model. One buzz cycle can be divided into three phases that correspond to the motions of the terminal shock. In the first phase, the terminal shock moves upstream due to the high backpressure, and the inlet starts to operate in a subcritical mode (1–2 of Fig. 17). This upstream movement goes up the point where the separation grows out to block the inlet section, according to the downstream flow condition (2–4 of Fig. 17). This causes the external flow to spill outside the cowl lip, while the entering mass flow and the pressure of the plenum chamber simultaneously decrease. As the terminal shock is expelled to near the tip of the compression surface, the separation bubble significantly blocks the inlet section (4–7 of Fig. 17). At the same time, the mass flow entering the inlet begins to decrease continuously, and the downstream pressure decreases as the blocking proceeds. After the downstream pressure has sufficiently decreased, the second phase starts. The terminal shock moves downstream again as the separation on the cone surface gradually disappears (8–12 of Fig. 17). The

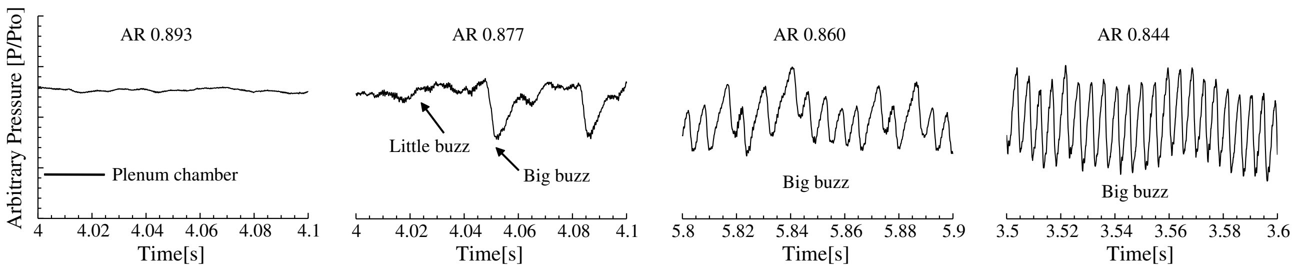

**a) Critical** **b) Intermittent buzz** **c) Continuous buzz** **d) Continuous buzz**

**Fig. 16 Pressure from critical to buzz modes for the rectangular model during a 0.1 s interval.**

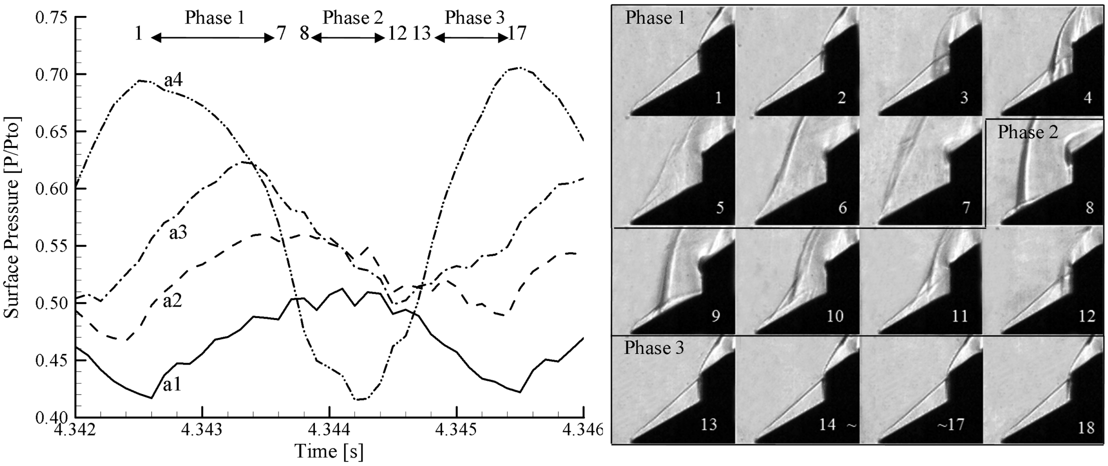

**Fig. 17 Pressure (left) and shadowgraph images (right) during one buzz cycle for the axisymmetric model.**

existence of separation bubble can be deduced by the variation of shock structure on the cone surface. When the terminal shock moves forward and backward, another oblique shock with different deflection angle is observed between the first oblique shock originated the cone surface and the terminal shock. This second oblique shock is generated by the separation bubble on the cone. As the separation bubble disappears and the entering mass flow increases, the pressure of the plenum chamber gradually increases as the flow fills the inside of the inlet. The inlet restarts as the terminal shock moves inside the inlet duct, which marks the start of the third phase. The inlet operates at the supercritical or critical mode until the terminal shock moves forward again (12–17 of Fig. 17). When the pressure of the plenum chamber becomes sufficiently large, the terminal shock is expelled from the cowl lip, the inlet is again in the subcritical mode, and a new cycle begins.

Figure 18 shows successive schlieren pictures that were taken during a buzz cycle for the rectangular model at AR = 0.828. From the external and internal images of Fig. 18, we can see the process by which the buzz develops. The schlieren images were obtained under the same conditions; thus, the time lapse between successive images is about 0.167 ms. The visualization region is marked by the dashed rectangular outline in the schematic diagram of the inlet (Fig. 18a). The shocks that should be ignored are marked as A and B at the top left and bottom right portions of the schlieren region, respectively, in the snapshot of Fig. 18b. The order of the pictures is marked by numbers, where 1 marks the beginning of the buzz cycle. Finally, the

**a) Visualization region using schlieren**

**b) External shocks that are not related to the internal flow (Note that A represents oblique shocks from nozzle tip and B represents shocks from external protuberances)**

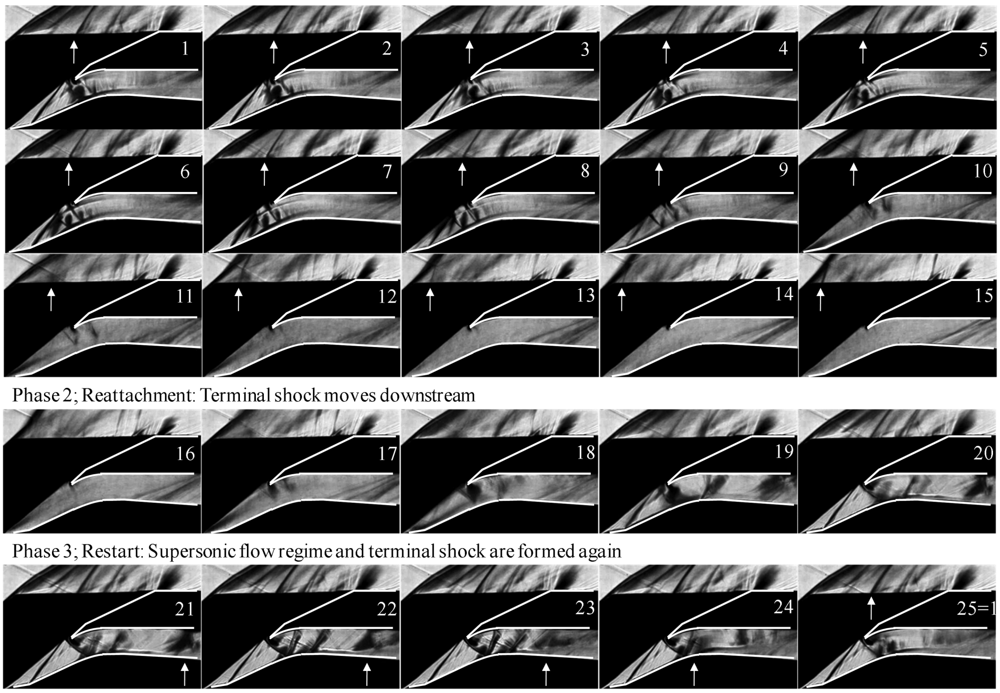
Phase 1; Subcritical to Unstart: Terminal shock moves upstream

Phase 2; Reattachment: Terminal shock moves downstream

Phase 3; Restart: Supersonic flow regime and terminal shock are formed again

**c) Visualization images during one cycle of buzz (Note that white arrows represent the position of moving terminal shocks)**

**Fig. 18 Schlieren visualization of a buzz cycle for the rectangular model (AR = 0.828).**

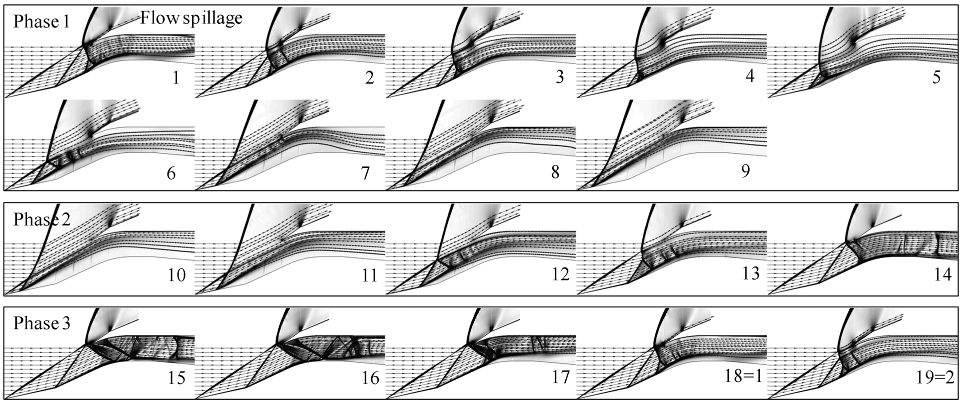

Fig. 19 Numerical schlieren images and streamlines for the rectangular model (AR = 0.828).

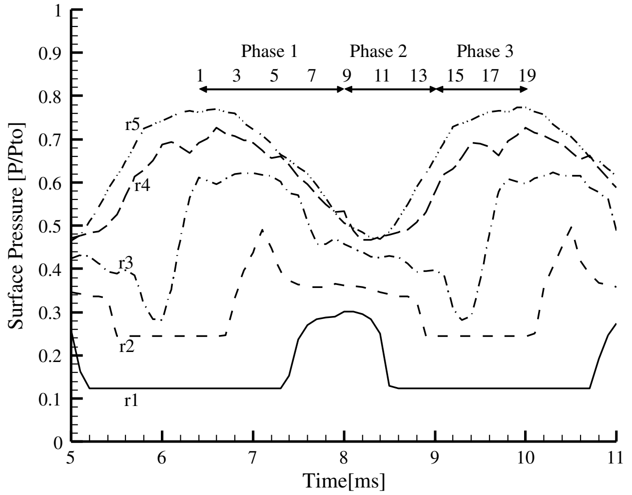

Fig. 20 Surface-pressure histories during a buzz cycle (the numbers correspond to the numbers of the snapshots in Fig. 19).

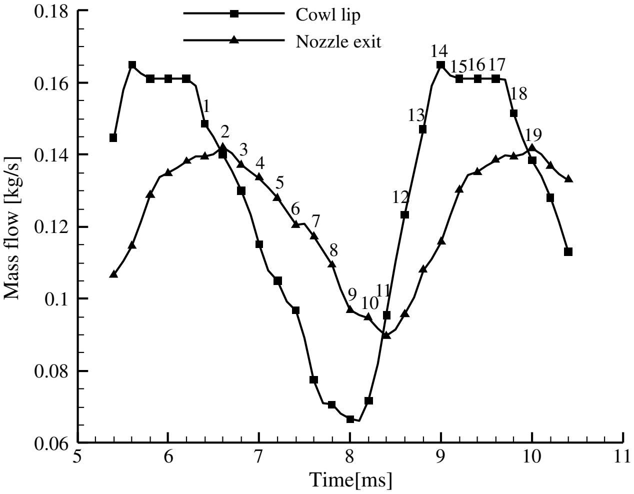

Fig. 21 Instantaneous mass flows at the cowl lip and nozzle exit section for snapshots 1–19 of Fig. 19.

white arrows represent the positions of the terminal shock. In the first picture, the terminal shock is expelled from the cowl lip and reaches its farthest point upstream after 13 frames; then, the terminal shock is almost motionless, as shown in frames 14–15. In frame 16, the terminal shock has moved back downstream, and a supersonic regime is formed again in frame 19. The oblique shocks are generated near the cowl lip and inlet throat as the supersonic regime is formed, and a terminal shock is formed again by high backpressure, as shown in frames 19–22. The terminal shock then moves upstream again, and a new cycle commences.

Figure 19 shows the numerical schlieren images during a buzz cycle with the streamlines added. The time lapse between two successive images is 0.2 ms. As mentioned before, the numerical results were overestimated to predict the pressure compared with the experimental results at the same AR. This tendency is also observed to predict the buzz phenomenon, for which the buzz frequency is also overestimated. For an AR of 0.828, the base frequency was variously estimated as 252.2 Hz from fast Fourier transformation (FFT) analysis of the measured pressure data, 250 Hz from the schlieren images taken during the experiments, and 294.1 Hz from the numerical analysis. Figure 20 depicts the surface-pressure histories over time for the buzz cycle shown in Fig. 19. The numbers correspond to the numbers of the snapshots in Fig. 19. Figure 21 shows the instantaneous mass inflow and outflow at the cowl lip and the nozzle exit, respectively, for snapshots 1–19 of Fig. 19. Although there is a small difference between the experimental and numerical sets of results, it is possible to more clearly explain the buzz phenomenon by using the two sets of results because they agree with the flow features.

According to these results, the observed buzz cycle can be characterized clearly.

For phase 1 (subcritical to unstart), as the terminal shock moves upstream due to the high pressure inside the inlet, flow spillage is observed outside of the cowl lip (1 of Figs. 18 and 19), and the rate of entering mass flow begins to decrease at the same time (1 of Fig. 21). Because of this high pressure, the terminal shock is expelled up to the first compression surface, and the external flow spillage becomes severe (2–9 of Fig. 18 and 2–5 of Fig. 19). This spillage causes the rate at which the mass flow enters to continuously decrease (1–5 of Fig. 21), and the pressure of the plenum chamber decreases, but the pressure of the inlet throat stays the same when the pressure decrease of the plenum chamber affects the inlet throat (3–7 of Fig. 20). As the terminal shock is expelled almost at the compression tip, the separated zone on the compression surface grows out and obstructs a significant part of the inlet section (10–15 of Fig. 18 and 6–9 of Fig. 19). Because of the obstruction, the rate at which the mass flow enters decreases sharply, and the pressure inside the inlet consequently decreases.

Table 1 Base frequencies at continuous buzz

| Axisymmetric model | | Rectangular model | |
|---|---|---|---|
| AR | Freq., Hz | AR | Freq., Hz |
| 0.806 | 312.5 | 0.828 | 252.2 |
| 0.704 | 375.0 | 0.762 | 358.0 |
| 0.651 | 384.6 | 0.697 | 379.3 |
| 0.598 | 420.1 | 0.631 | 417.5 |
| 0.449 | 447.8 | 0.565 | 444.7 |

Table 2 Characteristics of terminal shock motion and base frequency for rectangular model

| AR | 0.828 | 0.762 | 0.697 | 0.631 | 0.565 | 0.501 |
|---|---|---|---|---|---|---|
| Phases 1 and 3, forward-moving shock, ms | 3.0 | 1.76 | 1.6 | 1.32 | 1.14 | 1.04 |
| Phase 2, backward- moving shock, ms | 1.0 | 1.04 | 1.04 | 1.1 | 1.08 | 1.08 |
| Base freq. from schlieren images, Hz | 250 | 367.1 | 378.8 | 413.2 | 450.5 | 471.2 |
| Base freq. from pressure data, Hz | 252 | 368 | 378.3 | 417.5 | 444.7 | 468.7 |

For phase 2 (reattachment), when the pressure downstream from the shock is sufficiently low (9 of Fig. 20), the terminal shock moves back downstream and the shock-induced separation bubble on the compression surface gradually disappears (16–20 of Fig. 18 and 10–14 of Fig. 19). Thus, the inlet obstruction gradually disappears and the rate at which the mass flow enters increases (10–14 of Fig. 21). The pressure of the plenum chamber increases as the flow fills (10–14 of Fig. 20), and the terminal shock appears inside the inlet when the pressure inside the inlet becomes sufficiently high (20 of Fig. 18 and 14 of Fig. 19).

For phase 3 (restart), the inlet is operated as in supercritical conditions, although the AR is fixed below the critical value. The inlet entrance is not obstructed any longer (21–24 of Fig. 18 and 15–17 of Fig. 19), the mass flow entering rate remains at almost the maximum value (15–17 of Fig. 21), and the pressure inside the inlet continuously increases. The terminal shock moves forward due to the high pressure inside the inlet, and the flow becomes subcritical as the terminal shock is expelled (25 of Fig. 18 and 18 of Fig. 19).

### 3. *Buzz Frequencies*

When the inlet operates in the subcritical mode, the entrance flow is bypassed and the mass flow is regulated as the terminal shock oscillates slightly near the cowl lip. If the AR is slightly reduced while oscillating near the cowl lip in a subcritical mode (namely, a little buzz), the big buzz, which provides the oscillatory motion of the terminal shock, is much larger and is initiated intermittently and randomly. The reason for this intermittence and random behavior remains unclear, but this phenomenon might be related with acoustic stimulation, and two other causes are plausible. One cause could be a random pressure pulse downstream from the high backpressure. The other cause could be the internal air accumulation process with the reduction of the AR. Also, it is possible that the intermittent and random natures of the buzz may be the result of a combination of these two causes, and these phenomena were not observed for any AR in our numerical simulations. However, it is clear that the terminal shock moves further upstream due to the random pulse or the accumulation process, and the big buzz is initiated as the separation zone grows on the compression surface. If the AR is sufficiently low and the backpressure becomes too large, there is no duration for which the inlet operates at a subcritical mode or a little buzz, and the big buzz is initiated continuously and periodically since the motions of the terminal shock depend strongly on the backpressure.

The base frequencies of the little buzz for the subcritical mode are 386.7 and 518 Hz, as determined from the pressure distributions in Figs. 14 and 16 for both models. The fundamental acoustic modes for a duct with open and a closed ends are computed using Eq. (3) [29,41]:

$$f_n = (2n + 1)\frac{c}{4L}(1 - M^2) \qquad n = 0, 1, 2, \ldots \tag{3}$$

From the simulation results, the mean values between the subsonic diffuser and the flow choking section are as follows: $c = 327.1$ and $340.1\ \mathrm{m/s}$, $M = 0.33$ and $0.43$, and $L = 0.15$ and $0.113\ \mathrm{m}$ for axisymmetric and rectangular models, respectively. According to this formula, the calculated fundamental frequency is 488.7 Hz for the axisymmetric model and 610 Hz for the rectangular model. The difference in the fundamental frequencies for both models is mainly due to the length of inlet duct $L$, as shown in Fig. 1. The measured base frequency is less than the fundamental frequency of the acoustic resonance modes. As shown in Fig. 4, the separation bubble exists on the compression surface and the inlet throat for the subcritical conditions. It can be inferred that disturbances generated by the separation bubble make the base frequency different from the acoustic resonance of the inlet duct. Similar phenomena were observed by another author in experimental results at Mach 5 using a small-sized inlet and a duct length of 190 mm [42]. These phenomena were not observed in other studies that used a large model where the diffuser length was larger than 1 m [27–30,43]. Indeed, the unit Reynolds number of the inflow in all referred tests [27–30,42,43], including this study, is very similar to about $50–70 \times 10^6$, but only the size of the test model is different. This result means that the separation bubble can more sensitively affect the buzz characteristics of the small-sized supersonic inlet than a large-scale inlet.

The base frequency characteristics of the continuous buzz derived from a FFT analysis are shown in Table 1 for both models. The base frequencies for both models are very similar. In other words, if the inlet models have a similar total length and the same design process, the base frequencies of the buzz are the same, even though the shapes of the inlet models may differ. This result suggests that the buzz processes are very similar to each other and that the base frequency is

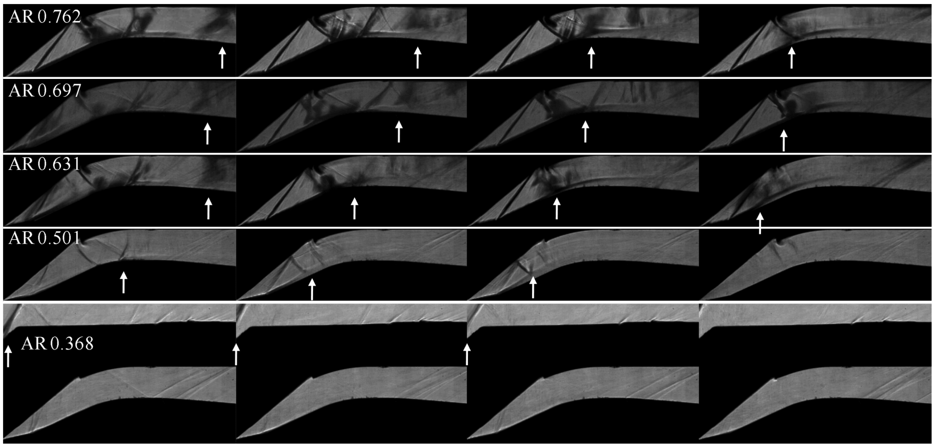

**Fig. 22 Flow features starting from the first instant in intervals of 2 ms during phase 3 of a buzz. (Note that white arrows represent the position of moving terminal shocks.)**

determined by the terminal shock motion that accompanies an acoustic phenomenon.

For the rectangular model, the time that it takes for the terminal shock to move upstream or downstream is summarized in Table 2. As the AR is reduced, the time for which the terminal shock moves backward is nearly constant, while the time that the shock moves forward decreases. This means that the time that it takes for the separation bubble to disappear does not significantly vary with AR values. This is the reason why the base frequency increases as the AR decreases, but this relationship is not linear. Consequently, the generation and extinction of the separation bubble on the compression surface and the inlet throat also play an important role in determining the base frequency of a continuous buzz, namely, a big buzz. Figure 22 shows the visualization images of phase 3 of the buzz cycle for various AR values. Although the terminal shock is formed at the subsonic diffuser, however, a supersonic flow is not perfectly formed inside the inlet. The position where the terminal shock is formed moves faster upstream as the AR decreases, and the restart phase, which forms a supersonic flow, gradually disappears. At $AR = 0.501$, the terminal shock is formed near the inlet throat at the restart phase, and the supersonic flow is not clearly formed, even on the compression surface. The terminal shock oscillates outside the inlet at $AR = 0.368$, and the inlet never restarts, as all regions inside the inlet remain subsonic.

## V. Conclusions

The wind-tunnel tests and computational simulations were conducted for the small-sized supersonic inlets. Two types of inlet models, axisymmetric and rectangular, which have similar total lengths of about 160 mm and were designed by the same method, were used. The tests were conducted while changing the throat area of the exit jet. Detailed visualization images for the entire process, from stable to unstable operation, were presented, and the flow characteristics around the small-sized inlet were understood in detail based on the results.

Similar to a conventional supersonic inlet, the main flow feature of the small-sized inlet was also the existence of the shock train during the stable operation. The results showed that the shock train could be differently generated by operating conditions including the size of the diffuser. The characteristics of the asymmetric shock train were mainly determined by the boundary layer that developed inside the diffuser, and the normal and oblique shock trains depended on the size of diffuser as well as the upstream Mach number of terminal shock. Various buzz phenomena were examined for unstable operation. The results showed that a little buzz was changed to a big buzz and a big buzz was initiated from intermittently to continuously as the throat area of the exit jet decreased. For a small-sized inlet, the existence of separation played an important role in determining the base frequency of both the little and big buzzes. The measured base frequency of the little buzz was different from that of the acoustic modes due to disturbances generated from the separation, and the phenomenon only appeared in the small-sized inlets. However, the processes or initiation mechanisms of the big buzz were identical to those reported previously, although the test model used in this study was very small. Also, the base frequencies for both models were at very similar levels during the continuous buzz, although the shapes of both inlets were different, verifying previous reports that explain how the buzz process is associated with acoustic waves moving back and forth in the diffuser. The buzz process was substantially impacted by the generation and extinction of a separation process on the compression surface and the inlet throat that was induced by the terminal shock.

This paper offers an in-depth investigation of the entire flow phenomena of the inlet, including the shock system, the shock/boundary-layer interaction, and the supersonic inlet buzz. These results will be very useful for engineers designing supersonic inlets. Moreover, the detailed images presented in this paper will be helpful for many researchers by enabling them to directly observe the entire process of inlet operation. Finally, the results can be useful for developing a small-sized supersonic inlet, such as an SFRJ.

## Acknowledgments

This work was supported by the second stage of the Brain Korea 21 Project at Seoul National University, the Defense Acquisition Program Administration, and the Agency for Defense Development, under the contract UD070041AD, and the Korea Science and Engineering Foundation grant funded by the Korea government (Ministry of Education, Science, and Technology).

## References

[1] Seddon, J., and Goldsmith, E. L., *Intake Aerodynamics*, AIAA Education Series, AIAA, New York, 1985, pp. 1–30.

[2] Mahoney, J. J., *Inlets for Supersonic Missiles*, AIAA Education Series, AIAA, Washington, D.C., 1990.

[3] Matsuo, K., Miyazato, Y., and Kim, H. D., "Shock Train and Pseudo-Shock Phenomena in Internal Gas Flows," *Progress in Aerospace Sciences*, Vol. 35, No. 1, Elsevier, New York, Jan. 1999, pp. 33–100. doi:10.1016/S0376-0421(98)00011-6

[4] Hong, J. W., "Experimental Investigation of Supersonic Nozzle Flow with Shock Wave/Turbulent Boundary Layer Interaction," Ph.D. Thesis, Department of Energy Conversion Engineering, Kyushu Univ., Fukuoka, Japan, Dec. 1995.

[5] Stockbridge, R. D., "Experimental Investigation of Shock Wave/Bboundary-Layer Interaction in an Annular Duct," AIAA Paper 1988-0272, 1988.

[6] Delery, J., and Marvin, J. G., "Shock Wave Boundary Layer Interactions," AGARD Rept. AG-280, Feb. 1986.

[7] Sajben, M., and Kroutil, J. C., "Effects of Initial Boundary-Layer Thickness on Transonic diffuser flows," *AIAA Journal*, Vol. 19, No. 11, 1981, pp. 1386–1393. doi:10.2514/3.60075

[8] Bogar, T. J., Sajben, M., and Kroutil, J. C., "Characteristic Frequencies of Transonic Diffuser Flow Oscillations," *AIAA Journal*, Vol. 21, No. 9, 1983, pp. 1232–1240. doi:10.2514/3.8234

[9] Sajben, M., Bogar, T. J., and Kroutil, J. C., "Experimental Study of Flows in a Two-dimensional Inlet Model," *Journal of Propulsion and Power*, Vol. 1, No. 2, March–April 1985, pp. 109–117. doi:10.2514/3.22767

[10] Carroll, B. F., and Dutton, J. C., "Characteristics of Multiple Shock Wave/Turbulent Boundary-Layer Interaction in Rectangular Ducts," *Journal of Propulsion and Power*, Vol. 6, No. 2, 1990, pp. 186–193. doi:10.2514/3.23243

[11] Hamed, A., and Shang, J. S., "Survey of Validation Data Base for Shockwave Boundary-Layer Interactions in Supersonic Inlets," *Journal of Propulsion and Power*, Vol. 7, No. 4, July–Aug. 1991, pp. 617–625. doi:10.2514/3.23370

[12] Talcott, N. A., Jr., and Kumar, A., "Two-Dimensional Viscous Simulation of Inlet/Diffuser Flows with Terminal Shocks," *Journal of Propulsion and Power*, Vol. 1, No. 2, March–April 1985, pp. 103–108. doi:10.2514/3.22766

[13] Hirschen, C., Herrmann, D., and Gülhan, A., "Experimental Investigations of the Performance and Unsteady Behavior of a Supersonic Intake," *Journal of Propulsion and Power*, Vol. 23, No. 3, May–June 2007, pp. 556–574. doi:10.2514/1.25103

[14] Chyu, W. J., Kawamura. T., and Bencze, D. P., "Navier–Stokes Solutions for Mixed Compression Axisymmetric Inlet Flow with Terminal Shock," *Journal of Propulsion and Power*, Vol. 5, No. 1, Jan.–Feb. 1989, pp. 4–5. doi:10.2514/3.23106

[15] Shigematsu, J., and Yamamoto, K., "A Numerical Investigation of Supersonic Inlet Using Implicit TVD Scheme," AIAA Paper 1990-2135, July 1990.

[16] Lin, P., Rao, G. V. R., and O'Connor, G. M., "Numerical Analysis of Normal Shock Train in a Constant Area Isolator," AIAA Paper 1991-2162, 1991.

[17] Hunter, L. G., Couch, B. D., "A CFD Study of Precombustion Shock-Trains for Mach 3–6," AIAA Paper 1990-2220, 1990.

[18] Oswatitsch, K., "Pressure Recovery for Missiles with Reaction Propulsion At High Supersonic Speeds (The Efficiency of Shock Diffusers)," Forschungen und Entwicklungen des Heereswaffenamtes, Rept. 1005, Göttingen, Germany, 1944.

[19] Ferri, A., and Nucci, L. M., "The Origin of Aerodynamic Instability of Supersonic Inlets at Subcritical Conditions," NACA RM L50K30, 1951.

[20] Dailey, C. L., "Supersonic Diffuser Instability," Ph.D. Thesis, California Inst. of Technology, Pasadena, CA, 1954.

[21] Hermann, R., "Supersonic Inlet Diffusers and Introduction to Internal Aerodynamics," Minneapolis-Honeywell Regulator Co., Wabash, IN, 1956, pp. 268–284.

[22] Sterbentz, W. H., and Evvard, J. C., "Criterion for Prediction and Control of Ramjet Flow Pulsations," NACA TN 3506, Aug. 1955.

[23] Trimpi, R. L., "An Analysis of Buzzing in Supersonic Ramjets by a Modified One-Dimensional Non-Stationary Wave Theory," NACA TN 3695, 1956.

[24] Connors, J. F., and Wollett, R. R., "Performance Characteristics of Several Types of Axially Symmetric Nose Inlets at Mach Number 3.85," NACA RM E52I15, Nov. 1952.

[25] Nagashima, T., Obokata, T., and Asanuma, T., "Experiment of Supersonic Intake Buzz," ISAS Rept. 481, Univ. of Tokyo, Tokyo, Japan, May 1972.

[26] Hongprapas, S., Kozak, J. D., Moses, B., and Ng, W. F., "A Small Scale Experiment for Investigating the Stability of a Supersonic Inlet," AIAA Paper 1997-0611, 1997.

[27] Lu, P. J., and Jain, L. T., " Numerical Investigation of Inlet Buzz Flow," *Journal of Propulsion and Power*, Vol. 14, No. 1, Jan.–Feb. 1988, pp. 1375–1379.
doi:10.2514/2.5254

[28] Fisher, S. A., Neale, M. C., and Brooks, A. J., "On the Sub-Critical Stability of Variable Ramp Intakes at Mach Numbers Around 2," National Gas Turbine Establishment Rept. ARC-R/M-3711, England, U.K., Feb. 1970.

[29] Trapier, S., Duveau, P., and Deck, S., "Experimental Study of Supersonic Inlet Buzz," *AIAA Journal*, Vol. 44, No. 10, Oct. 2006, pp. 2354–2365.
doi:10.2514/1.20451

[30] Trapier, S., Deck, S., and Duveau, P., "Delayed Detached-Eddy Simulation and Analysis of Supersonic Inlet buzz," *AIAA Journal*, Vol. 46, No. 1, Jan. 2008, pp. 118–131.
doi:10.2514/1.32187

[31] Andersson, K., "SOFRAM-Report of Completed Firing Tests During 2000, Along with a Review of Former Activities and Discussion of the Future," FOI-Swedish Defence Research Agency, FOI-R-0241-SE, Stockholm, Oct. 2001.

[32] Veraar, R. G., and Mayer, A. E. H. J., "The Role of the TNO Free Jet Test Facility in Solid Fuel Ramjet Projectile Development," AIAA Paper 2005-3828, 2005.

[33] Krishnan, S., and Philmon, G., "Solid Fuel Ramjet Combustor Design," *Progress in Aerospace Sciences*, Vol. 34, Nos. 3–4, 1998, pp. 219–256.
doi:10.1016/S0376-0421(98)00005-0

[34] Lee, H. J., Kim, S. D., and Jeung, I. S., "Experimental Study on the Supersonic Inlet buzz with Angle of Attack," 18th International Symposium on Airbreathing Engines, Beijing, ISABE Paper 2007-1211, Sept. 2007.

[35] Oswatitsch, K., "Pressure Recovery for Missiles with Reaction Propulsion at High Supersonic Speeds," NACA TM 1140, 1948.

[36] Settles, G. S., *Schlieren and Shadowgraph Techniques*, Springer–Verlag, New York, 2001.

[37] Menter, F. R., "Two-Equation Eddy-Viscosity Turbulence Models for Engineering Applications," *AIAA Journal*, Vol. 32, No. 8, 1994, pp. 1598–1605.
doi:10.2514/3.12149

[38] Hoffmann, K. A., *Computational Fluid Dynamics*, Engineering Education System, Wichita, KS, 2000.

[39] Roe, P. L., "Approximate Reimann Solvers, Parameter Vectors and Difference Scheme," *Journal of Computational Physics*, Vol. 43, No. 2, 1981, pp. 357–372.
doi:10.1016/0021-9991(81)90128-5

[40] Chakravarthy, S. R., and Osher, S., "A New Class of High Accuracy TVD Schemes for Hyperbolic Conservation Laws," AIAA Paper 1985-0363, Jan. 1985.

[41] Newsome, R. W., "Numerical Simulation of Near-Critical and Unsteady, Subcritical Inlet Flow," *AIAA Journal*, Vol. 22, No. 10, 1984, pp. 1375–1379.
doi:10.2514/3.48577

[42] Tan, H., Sun, S., and Yin, Z., "Oscillatory Flows of Rectangular Hypersonic Inlet Unstart Caused by Downstream Mass-Flow Choking," *Journal of Propulsion and Power*, Vol. 25, No. 1, Jan. 2009, pp. 138–147.
doi:10.2514/1.37914

[43] Vivek, P., and Mittal, S., "Buzz Instability in a Mixed-Compression Air Intake," *Journal of Propulsion and Power*, Vol. 25, No. 3, May 2009, pp. 819–822.
doi:10.2514/1.39751

F. Liu
*Associate Editor*